Atmos. Chem. Phys., 9, 3061–3073, 2009
www.atmos-chem-phys.net/9/3061/2009/


Atmospheric Chemistry and Physics

# A simulation of the global distribution and radiative forcing of soil dust aerosols at the Last Glacial Maximum

**T. Takemura**[1], **M. Egashira**[2], **K. Matsuzawa**[2], **H. Ichijo**[3], **R. O'ishi**[3], **and A. Abe-Ouchi**[3]

[1]Research Institute for Applied Mechanics, Kyushu University, Fukuoka, Japan
[2]Interdisciplinary Graduate School of Engineering Sciences, Kyushu Univ., Fukuoka, Japan
[3]Center for Climate System Research, University of Tokyo, Chiba, Japan

Received: 12 September 2008 – Published in Atmos. Chem. Phys. Discuss.: 9 December 2008
Revised: 26 February 2009 – Accepted: 8 May 2009 – Published: 13 May 2009

**Abstract.** In this study an integrated simulation of the global distribution and the radiative forcing of soil dust aerosols at the Last Glacial Maximum (LGM) is performed with an aerosol climate model, SPRINTARS. It is compared with another simulation for the present climate condition. The global total emission flux of soil dust aerosols at the LGM is simulated to be about 2.4 times as large as that in the present climate, and the simulated deposition flux is in general agreement with estimations from ice core and marine sediment samplings though it appears to be underestimated over the Antarctic. The calculated direct radiative forcings of soil dust aerosols at the LGM is close to zero at the tropopause and $-0.4\,\mathrm{W\,m^{-2}}$ at the surface. These radiative forcings are about twice as large as those in the present climate. SPRINTARS also includes the microphysical parameterizations of the cloud-aerosol interaction both for liquid water and ice crystals, which affect the radiation budget. The positive radiative forcing from the indirect effect of soil dust aerosols is mainly caused by their properties to act as ice nuclei. This effect is simulated to be smaller ($-0.9\,\mathrm{W\,m^{-2}}$) at the LGM than in the present. It is suggested that atmospheric dust might contribute to the cold climate during the glacial periods both through the direct and indirect effects, relative to the interglacial periods.

## 1 Introduction

The air temperature during the glacial and interglacial periods has been analyzed with ice cores, marine sediments, and pollens. The annual mean surface air temperature is 3 to 6 K lower on the global mean at the Last Glacial Maximum (LGM), which is about twenty-one thousands years ago, than in the present climate (Jouzel et al., 1993; Kucera et al., 2005; Masson-Delmotte et al., 2005; Wu et al., 2007; Otto-Bliesner et al., 2009). It is regionally about 3 and 10 K lower over the tropics and southern Europe, respectively. It is, however, impossible to quantitatively explain the remarkable low temperature and extended ice sheets at the LGM only with the change in the insolation. It is now accepted that a combination of lower greenhouse gas concentrations, extended ice sheets, and feedback mechanisms within and among the atmosphere, ocean, cryosphere, and vegetation played important roles in the LGM climate. Based on simulations from the Paleoclimate Modeling Intercomparison Project 2 (PMIP2) (Braconnot et al., 2007), Jansen et al. (2007) reported the radiative perturbation at the LGM to be $-4$ to $-7\,\mathrm{W\,m^{-2}}$ relative to the pre-industrial (1750) climate due to lower greenhouse gas concentrations, extended continental ice, and lower sea level than the present climate. This range for the perturbation does not include the effects of vegetation and aerosol changes. The scientific understanding of the radiative perturbation due to atmospheric mineral dust is very low.

Analyses of ice cores and sediments have shown that the deposition flux of atmospheric soil dust aerosols varied between the glacial and interglacial periods (Petit et al., 1999). Soil dust aerosols are considered as one of the factors inducing climate change principally through two effects. One is the direct effect in which they scatter and absorb the solar and thermal radiation. The other is the indirect effect in which they alter the microphysical and optical properties of cloud droplets and ice crystals acting as cloud condensation nuclei (CCN) and ice nuclei (IN). Soil dust is one of the essential aerosols for IN although it has less effect for CCN because of

*Correspondence to:* T. Takemura
(toshi@riam.kyushu-u.ac.jp)

its hydrophobicity which does not favor internal mixing with other aerosols. The aerosol semi-direct effect is related to the absorption of solar and/or thermal radiation, such as soil dust, warm the surrounding atmosphere, resulting in changes in the atmospheric stability and cloud production. Therefore the difference in the concentration of soil dust aerosols between the glacial and interglacial periods may contribute to the large difference in the climate condition between them. Petit et al. (1999) indicated that the concentration of soil dust aerosols in the ice core from Vostok, Antarctica is one order-of-magnitude larger during the glacial than interglacial periods, especially at the LGM. The data from marine sediments also show that dust fluxes from Africa transported to the tropical and subtropical Atlantic at the LGM are three to five times higher than the present-day (Harrison et al., 2001). The increase of the soil dust concentration at the LGM may be assigned to the less precipitation, expansion of land areas, and strong winds.

Several modeling studies have simulated and analyzed the soil dust emission, concentration, and deposition at the LGM. Joussaume (1993) investigated the desert dust cycle in the LGM with an atmospheric general circulation model (AGCM), however only a weak increase in the dust emission was simulated. Andersen et al. (1998) simulated larger dust amounts during the LGM compared to present-day almost everywhere over the globe as a consequence of variations in soil moisture. The simulated deposition rates are still lower than the ones reported from ice cores. They indicated that inclusion of more realistic boundary conditions for the dust emission (e.g., vegetation) could also improve the LGM dust cycle. Indeed, Mahowald et al. (1999) showed that the simulated dust deposition flux at the LGM were roughly in agreement with observed data from marine sediments and ice cores by including a more realistic representation of the vegetation during the LGM. They showed that changes in source areas are required to predict any substantial increase in the dust deposition over the polar regions. Werner et al. (2002) suggested from their simulation that one third of the increase in the total global dust emission flux in the LGM is related to source-region changes, while two thirds is caused by glacial wind speed changes over modern dust emission regions. Mahowald et al. (2006) indicated that low $CO_2$ concentration at the LGM resulted in expanding dust sources through less fertilization of vegetation. The previous studies mentioned above have improved the understanding of the atmospheric dust condition at the LGM by numerical simulations. However, they concerned the dust distribution at the LGM, not its radiative impact.

Soil dust aerosols affect the radiation budget through the direct and indirect effects as mentioned above, so that they may have important potential to have an impact on the climate system in the glacial period. The PMIP2, however, did not treat the dust effects on the climate system. Claquin et al. (2003) calculated a difference in the direct radiative forcing of dust between the LGM and present conditions based on Mahowald et al. (1999). They estimated its global and annual mean value to be about $-2.0\,\mathrm{W\,m^{-2}}$ at the top of the atmosphere without the indirect effect. In this study, the radiative forcings both of the direct and indirect effects by soil dust aerosols at the LGM are calculated with a global aerosol climate model, Spectral Radiation-Transport Model for Aerosol Species (SPRINTARS), which is accompanied by the simulation of global distributions for main tropospheric aerosols. One of the significant improvement brought by this study is the inclusion of the interaction between ice crystals and aerosol particles in order to calculate the aerosol indirect effect. The model description is given in Sect. 2. Section 3 shows the simulated emission, distribution, and deposition of soil dust aerosols as well as sea salt aerosols both at the LGM and present-day. The simulated deposition fluxes of soil dust aerosols are compared with their estimations from ice cores and marine sediments in order to evaluate the performance and problems of the present model. Section 4 presents the calculated direct and indirect radiative forcings of soil dust aerosols and discuss their effects on the climate system at the LGM. This study is concluded in Sect. 5.

## 2 Model description

In this study, global distributions and radiative forcings of aerosol particles in the LGM climate condition are simulated by SPRINTARS (Takemura et al., 2000, 2002, 2005). It is fully coupled with an AGCM developed by the Center for Climate System Research (CCSR)/University of Tokyo, National Institute for Environmental Studies (NIES), and Frontier Research Center for Global Change (FRCGC) (K-1 Model Developers, 2004). The horizontal resolution used is T42 (approximately 2.8° by 2.8° in latitude and longitude) and the vertical resolution is 20 layers (sigma levels based on the surface pressure at 0.995, 0.980, 0.950, 0.900, 0.830, 0.745, 0.650, 0.549, 0.454, 0.369, 0.295, 0.230, 0.175, 0.124, 0.085, 0.060, 0.045, 0.035, 0.025, and 0.008). The standard time step is 20 min.

SPRINTARS predicts mass mixing ratios of the main tropospheric aerosols, that is, carbonaceous (black carbon (BC) and organic carbon (OC)), sulfate, soil dust, and sea salt, and the precursor gases of sulfate, that is, sulfur dioxide ($SO_2$) and dimethylsulfide (DMS). The aerosol transport processes include emission, advection, diffusion, sulfur chemistry, wet deposition, dry deposition, and gravitational settling. The emission flux of soil dust aerosols depends on the near-surface wind speed, vegetation, leaf area index (LAI), soil moisture, and snow amount (see Appendix A). The other natural emissions included in this study is sea salt aerosols (see Appendix B), BC, OC, and $SO_2$ from biomass burning, OC from the gas-to-particle conversion of terpene (Guenther et al., 1995), and dimethylsulfide (DMS) from oceanic phytoplankton and land. The global distribution of emission for biomass burning BC is based on the monthly mean data of the

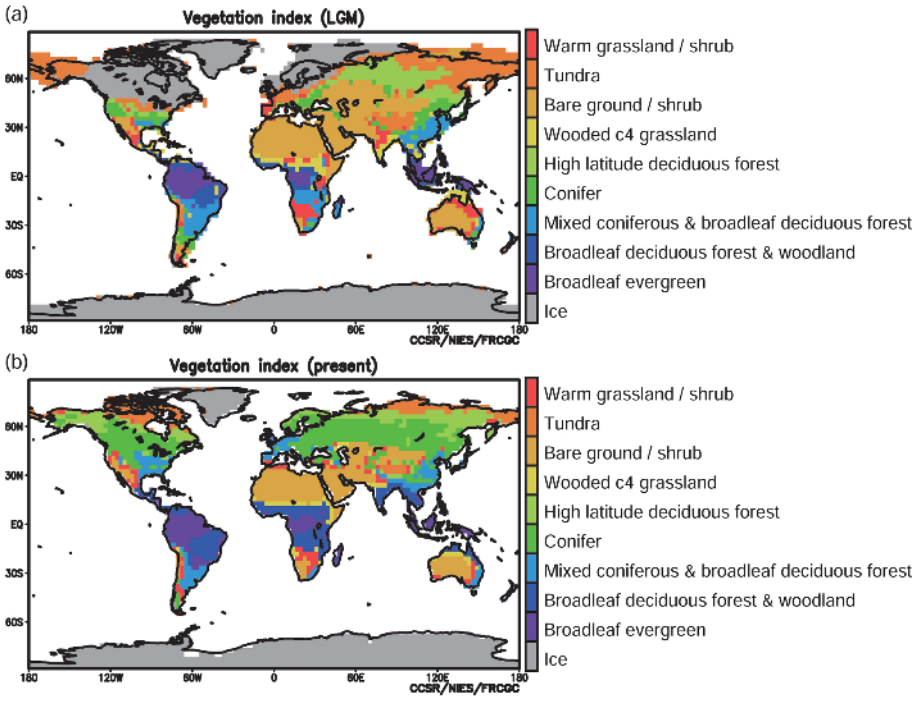


**Fig. 1.** Distributions of the vegetation in **(a)** LGM and **(b)** PRE.

Global Fire Emissions Database version 2 (GFEDv2) from the year 1997 to 2006 (Randerson et al., 2005), and the natural sources are assumed to be 10% of the total GFEDv2 emission (Andreae, 1991). The natural emissions of BC and OC mentioned above are assumed to be the same between the simulations for the LGM and a present climate condition. Differences in BC and OC emissions from natural sources between glacial and interglacial periods should be considered in future studies. A scheme of the DMS emission from oceanic phytoplankton which is a function of the downward surface solar radiation is the same as Takemura et al. (2000) and that from land vegetation and soil which is function of LAI, solar zenith angle, and temperature is according to Spiro et al. (1992). The other transport processes are according to Takemura et al. (2000, 2002, 2005).

The radiation scheme in the CCSR/NIES/FRCGC AGCM, which adopts the two-stream discrete ordinate and adding method (Nakajima et al., 2000), includes the calculation of the aerosol direct effect. The refractive indices depending on wavelengths, size distributions, and hygroscopic growth are considered for each type of aerosol. The refractive indices of dry aerosols and water are according to Deepak and Gerber (1983) and d'Almeida et al. (1991), respectively, except the imaginary part of soil dust aerosols which is a quarter of values in Deepak and Gerber (1983) because their weaker absorption of the solar radiation has been recently reported (e.g., Kaufman et al., 2001). The detailed description of the aerosol direct effect in SPRINTARS is in Takemura et al. (2002, 2005). An effect of dust deposition on the snow albedo change is not included in this study.

The aerosol indirect effect is also included both for water and ice clouds in SPRINTARS. The cloud droplet and ice crystal number concentrations are prognostic variables. The nucleation of the cloud droplets depends not only on the aerosol particle number concentrations but also on the size distributions, curvature effect, and solute effect of each type of aerosol, and the updraft velocity. The nucleation of the ice crystals includes both homogeneous and heterogeneous processes (see Appendix C). The growth and collision processes for cloud droplets and ice crystals are described also in Appendix C. Changes in the cloud droplet and ice crystal number concentrations induce changes in the cloud droplet and ice crystal effective radii, respectively, that is the first indirect effect, which result in a change in the radiation budget. The precipitation rate for warm rain is treated according to Berry's parameterization (Berry, 1967). It depends on the cloud droplet number concentration, that is the second indirect effect. The detailed description of the aerosol indirect effect for water clouds in SPRINTARS is in Takemura et al. (2005). Note that a change in the precipitation rate for cold rain is not included in the present version of SPRINTARS.

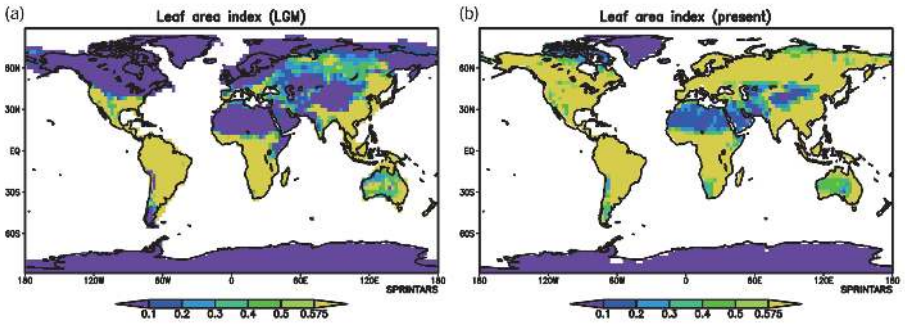


**Fig. 2.** Annual mean distributions of the leaf area index in **(a)** LGM and **(b)** PRE.

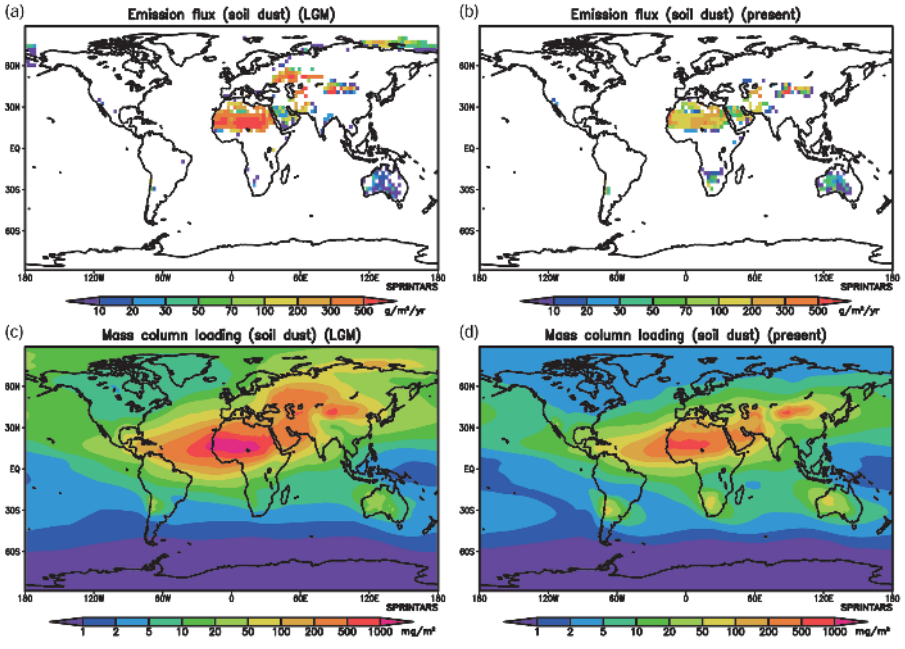


**Fig. 3.** Annual total distributions of the emission flux of soil dust aerosols in **(a)** LGM and **(b)** PRE and annual mean distributions of the mass column loading of soil dust aerosols in **(c)** LGM and **(d)** PRE.

The vegetation and monthly mean LAI distributions are prescribed with the simulation by the CCSR/NIES/FRCGC AGCM coupled with the Lund-Potsdam-Jena Dynamic Global Vegetation Model (LPJ-DGVM) (Sitch et al., 2003; Gerten et al., 2004). The potential vegetation types for dust emission are wooded c4 grassland, bare ground/shrub, tundra, and warm grassland/shrub in this study (Fig. 1). The bare ground/shrub in the LGM expands over the inland Asia, Middle and Near East, and southern Sahara in comparison with the present condition. The tundra also increases in the LGM, which is partly due to expansion of land because of the lower sea level, although there are large-scale ice sheets over the North America and Northern Europe. The prescribed vegetation distribution in the LGM is confirmed to be in general agreement with reconstruction data (Harrison and Prentice, 2003). Figure 2 shows the annual mean LAI distribution, and it is possible to emit soil dust aerosols if the LAI is less than about 0.575 according to Eqs. (A3)–(A4).

The initial condition and the climatological monthly mean data of sea surface temperature (SST) and sea ice in the LGM are prescribed from the results of the LGM simulation using the CCSR/NIES/FRCGC atmosphere-ocean coupled general circulation model (AOGCM), MIROC (Model for Interdisciplinary Research on Climate) (Yanase and Abe-

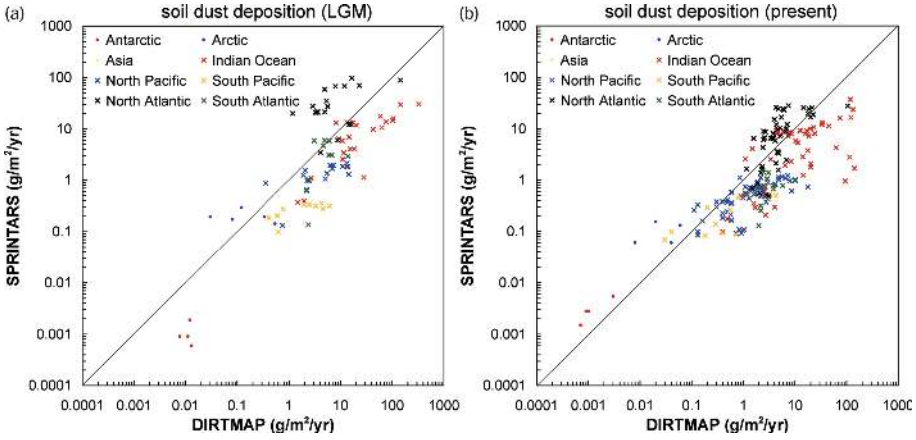


**Fig. 4.** Comparisons of annual total deposition flux of soil dust aerosols between the DIRTMAP database and SPRINTARS simulation in **(a)** LGM and **(b)** PRE. Dots and crosses show comparisons with DIRTMAP from ice cores and marine sediments, respectively.

Ouchi, 2007) which took part in the PMIP2 Project (Braconnot et al., 2007). The model result shows about 2.5 to 3 K SST change in the low latitude and about 5 K global change, which is in the range of uncertainty of climate reconstructions from different proxies and also comparable to the performance of other coupled AOGCMs in PMIP2 (Masson-Delmotte et al., 2005; Kageyama et al., 2006; Otto-Bliesner et al., 2009). As a reference simulation SPRINTARS also calculates global distributions and radiative forcings of aerosols in the pre-industrial era as a present climate condition (PRE). The HadISST data set (Rayner et al., 2003) averaged from the year 1870 to 1879 is used as the monthly SST and sea ice in the PRE simulation. The solar radiative flux at the top of the atmosphere is calculated with the eccentricity, obliquity of the earth's axis, and longitude of perihelion for the present and LGM time slices (Table 1). The atmospheric $CO_2$, $N_2O$, and $CH_4$ concentration are set to be constant globally and annually for the pre-industrial and LGM time slices (Table 1). Each experiment is integrated for 6 years and analyzed for the last 5 years.

## 3 Aerosol emission, distribution, and deposition in the LGM experiment

Figure 3a and b shows simulated global distributions of the annual dust emission at LGM and PRE, respectively. During PRE, the main emission sources are distributed between 50° N to 40° S: over the Sahara, the Middle East, Central Asia, the Kalahari Desert, Patagonia, and Australia. At LGM, sources expand southward over the Sahara and northward over Eastern Europe and Central Asia due to extended arid regions (Fig. 1). Other sources appear over northern Siberia during the glacial period because of the more extensive exposed continental shelves resulting from the sea level falling. As well as expansion of emission sources, the dust emission flux is also larger over the Sahara, the Middle and Near East, Asia, and Europe during LGM compared to PRE (Table 2). The global total flux in LGM is calculated to be 6200 Tg/yr, about 2.4 times as large as in PRE conditions. Werner et al. (2002) estimated a 2.2-fold higher dust emission flux at LGM compared to PRE, which is close to this study, though their estimation of the total LGM flux was smaller (2383 Tg/yr). The dust emission flux under the present climate condition is estimated to be 2594 Tg/yr in this study, which is in agreement with most past studies, ranging about from 1500 to 3000 Tg/yr (e.g., Tegen and Fung, 1994; Dentener et al., 1996; Chin et al., 2002; Tanaka and Chiba, 2005), while Werner et al. (2002) estimated it to be 1060 Tg/yr.

**Table 1.** Earth's planetary constants and main greenhouse gas concentrations in LGM and PRE.

| | LGM | PRE |
|---|---|---|
| Eccentricity | 0.018994 | 0.016720 |
| Obliquity of the earth's axis, degrees | 22.949 | 23.450 |
| Longitude of perihelion, degrees | 114.42 | 102.04 |
| $CO_2$, ppm | 185 | 287.96 |
| $N_2O$, ppb | 200 | 281.30 |
| $CH_4$, ppb | 350 | 902.48 |

Reasons for the high dust emission flux at LGM could be due not only to expansion of emission sources but also to stronger winds during this period. In order to separate the influence of extended arid regions from the other meteorological factors on the dust emission flux, an additional experiment (LGMfv) is performed with the present-day vegetation distribution as shown in Fig. 1b and with the same LGM conditions for other factors. Table 2 shows that the large emission flux of soil dust aerosols for LGM is more affected by

**Table 2.** Regional and global total annual emission fluxes of soil dust aerosols in LGM, PRE, and LGMfv and their ratio of LGM to PRE.

| Region | LGM, Tg/yr | PRE, Tg/yr | LGM/PRE | LGMfv, Tg/yr |
|---|---|---|---|---|
| Sahara | 4200 | 1692 | 2.48 | 3629 |
| Middle and Near East | 734 | 447 | 1.64 | 698 |
| Asia and Europe | 1187 | 273 | 4.36 | 311 |
| Australia | 48 | 83 | 0.58 | 91 |
| North America | 1.6 | 3.8 | 0.41 | 1.4 |
| South America | 16 | 48 | 0.33 | 44 |
| Southern Africa | 12 | 48 | 0.26 | 16 |
| Total | 6200 | 2594 | 2.39 | 4790 |

**Table 3.** Zonal and global total mass column loading and deposition fluxes of soil dust aerosols in LGM and PRE and their ratio of LGM to PRE. Numbers in parentheses in the deposition fluxes are percentages of the wet deposition fluxes to the total ones.

| | Mass column loading | | | Deposition | | |
|---|---|---|---|---|---|---|
| Latitude | LGM, Tg | PRE, Tg | LGM/PRE | LGM, Tg/yr | PRE, Tg/yr | LGM/PRE |
| 90° N–60° N | 0.77 | 0.11 | 6.80 | 143 (38%) | 6.5 (93%) | 21.9 |
| 60° N–30° N | 6.90 | 2.69 | 2.57 | 1586 (23%) | 536 (32%) | 2.96 |
| 30° N–0° | 21.47 | 9.35 | 2.29 | 4345 (13%) | 1858 (15%) | 2.34 |
| 0°–30° S | 1.49 | 1.13 | 1.32 | 110 (28%) | 156 (16%) | 0.71 |
| 30° S–60° S | 0.18 | 0.29 | 0.62 | 15 (65%) | 37 (57%) | 0.41 |
| 60° S–90° S | 0.02 | 0.02 | 1.20 | 0.2 (95%) | 0.4 (96%) | 0.50 |
| Total | 30.84 | 13.60 | 2.27 | 6200 (17%) | 2594 (19%) | 2.39 |

the meteorological condition than the vegetation over the Sahara and Middle and Near East, and vice versa over Asia and Europe. The simulation suggests that about 60% of the increase in the global total dust emission at LGM relative to PRE is due to a difference in the meteorological conditions, especially the strong winds and less precipitation, and the other is due to a difference in vegetation. These contributions to the increase in LGM dust emissions are close to the ones computed by Werner et al. (2002).

Figure 3c and d shows simulated global distributions of the annual mean dust column loading at LGM and PRE, respectively, and Table 3 shows zonal column loading and deposition flux of soil dust aerosols. When emitted from the Sahara, dust aerosols are transported to the West by the trade winds and when emitted from Asia to the East by the westerlies. The atmospheric dust loading is larger during the LGM than at PRE all over the Northern Hemisphere, especially in the high latitudes mainly due to the expansion of the emission sources. The distribution of the dust deposition flux is similar to that of the mass column burden (not shown). The zonal mean mass burden and deposition flux at LGM are respectively about 7 and 20 times as large as those at present between 90° N and 60° N, and 2 to 3 times between 60° N to 0°. The ratio of the dry to the total deposition flux is high near the source regions, and the wet deposition becomes a predominant deposition process away from the sources. One of the simulated characteristics at LGM is a high ratio of the dry deposition at northern high latitudes. The ratio of the dry to total deposition is also larger at LGM for low- and mid-latitude of the Northern Hemisphere than in present conditions because of the drier atmospheric conditions during LGM as well as the larger mass column loading at that time.

The simulated dust deposition fluxes for both LGM and PRE are compared with the DIRTMAP (Dust Indicators and Records of Terrestrial and Marine Palaeoenvironments) database (Kohfeld and Harrison, 2001), which includes deposition estimates from ice cores and marine sediments. It is to our knowledge the most complete database to compare simulated results with, though there are uncertainties. For example, fluxes from ice cores rely on estimates of ice accumulation rate in the cores which we cannot correct for the subtantial amount of dust that is advected by ocean currents (Kohfeld and Harrison, 2001; Mahowald et al., 2006). The DIRTMAP database suggests that tropical and mid-latitudes dust deposition fluxes are 2 to 5 times larger during the LGM than during interglacial periods, and over 20 times larger in the polar regions. Figure 4 shows comparisons of the annual dust deposition fluxes between DIRTMAP and the simulation by SPRINTARS for LGM and PRE. They are in general agreement in PRE, though there is a little underestimation over the Indian Ocean. Also, the LGM simulation generally

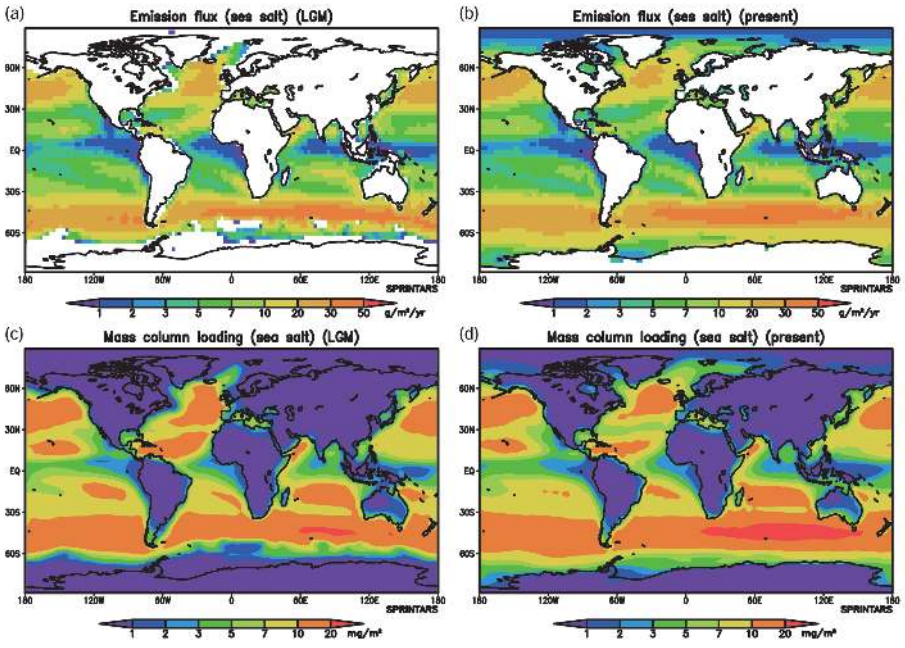


**Fig. 5.** Annual total distributions of the emission flux of sea salt aerosols in **(a)** LGM and **(b)** PRE and annual mean distributions of the mass column loading of sea salt aerosols in **(c)** LGM and **(d)** PRE.

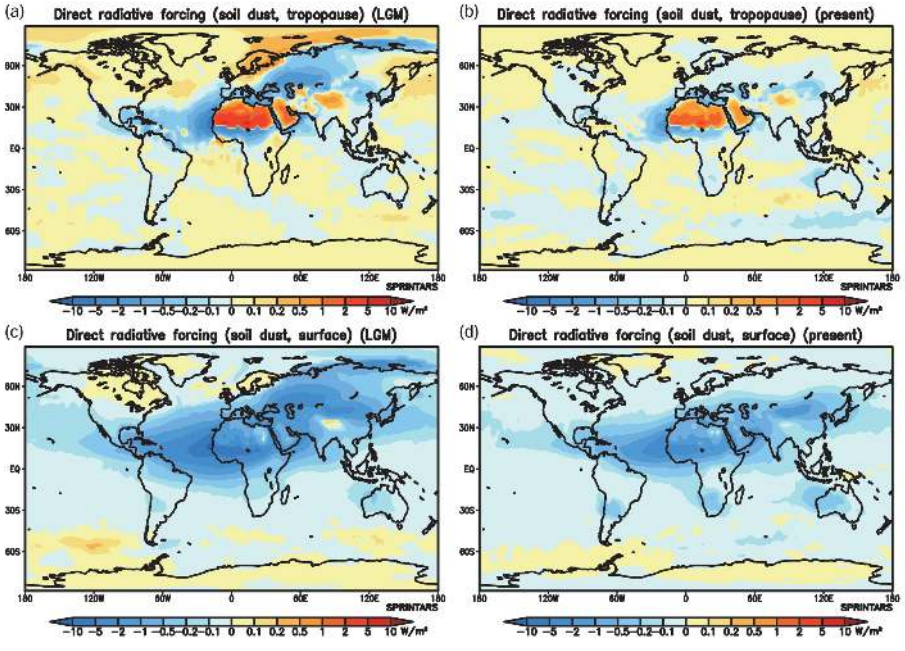


**Fig. 6.** Annual mean distributions of radiative forcing for the shortwave plus longwave radiation due to the direct effect of soil dust aerosols under the all-sky condition at the tropopause in the **(a)** LGM and **(b)** PRE and at the surface in **(c)** LGM and **(d)** PRE.

**Table 4.** Zonal and global total annual emission fluxes of sea salt aerosols in LGM and PRE, and their ratio of LGM to PRE.

| Latitude | LGM, Tg/yr | PRE, Tg/yr | LGM/PRE |
|---|---|---|---|
| 90° N–60° N | 21 | 76 | 0.27 |
| 60° N–30° N | 638 | 697 | 0.91 |
| 30° N–0° | 502 | 488 | 1.03 |
| 0°–30° S | 554 | 539 | 1.03 |
| 30° S–60° S | 1693 | 1963 | 0.86 |
| 60° S–90° N | 26 | 191 | 0.14 |
| Total | 3433 | 3955 | 0.87 |

**Table 5.** Global and annual mean radiative forcing for the direct effect of soil dust aerosols at the tropopause and surface under clear-sky and all-sky conditions in LGM and PRE. SW, LW, and SW+LW are shortwave, longwave, and shortwave plus longwave radiations, respectively.

| | Tropopause, W m$^{-2}$ | | | Surface, W m$^{-2}$ | | |
|---|---|---|---|---|---|---|
| | SW | LW | SW+LW | SW | LW | SW+LW |
| Clear-sky | | | | | | |
| LGM | −0.38 | +0.26 | −0.12 | −1.02 | +0.53 | −0.50 |
| PRE | −0.18 | +0.11 | −0.07 | −0.46 | +0.22 | −0.24 |
| All-sky | | | | | | |
| LGM | −0.24 | +0.22 | −0.02 | −0.88 | +0.45 | −0.43 |
| PRE | −0.10 | +0.09 | −0.01 | −0.38 | +0.18 | −0.20 |

captures the five order of magnitude range in the deposition fluxes although it underestimates the fluxes over Antarctica. Isotopic measurements from dust collected in ice-cores have suggested that dust deposited over Antarctica have a primary source over Patagonia whereas smaller amounts (10 to 15%) could be traced to Southern Africa and/or Australia (Basile et al., 1997). There are three possible reasons for the underestimation of dust emission from Patagonia in the LGM simulation from this study presented in Fig. 3 and Table 2. First, the large difference in the emission flux from the South America between LGM and LGMfv could be due to inappropriate vegetation indices and an underestimation of emerging land as a consequence of the fall in sea level. The second cause could be an underestimation of the wind intensity because the emission flux in LGMfv experiment is smaller than in PRE, in constrast to the behavior in the Northern Hemisphere. The other reason could be the underestimation of precipitation because the deposition flux over the high latitudes of the Southern Hemisphere at LGM is half of the deposition flux at PRE despite a mass burden during the LGM being somewhat larger than that at present and because the wet deposition is a primary process in the total dust deposition as indicated in Table 3.

The other principal natural aerosol is sea salt. Figure 5 shows simulated distributions of the annual emission flux and annual mean mass column loading of sea salt aerosols, and Table 4 presents their zonal and global total emission fluxes at LGM and PRE. Both the LGM emission flux and atmospheric burden in the tropics and at mid-laitudes are similar to those at PRE, though the LGM emission flux is slightly larger due to stronger winds. In constrast, the high-latitudes emission is prevented by the extended sea ice in LGM conditions.

## 4 Dust radiative forcing in the LGM experiment

The direct radiative forcing of soil dust aerosols is calculated as the difference in the radiative budget between the inclusion and the exclusion of soil dust aerosol within the same simulation. Figure 6 shows the annual mean distributions of the direct radiative forcing due to soil dust aerosols under the all-sky condition. The forcing at the tropopause is negative over most oceanic and forest areas, while it is positive over arid regions due to high surface albedo. Even over the ocean where the surface albedo is low, it is partly positive, in spite of small values, because soil dust aerosols absorb the solar radiation scattered by the lower cloud layer than the dust layer as well as the direct solar radiation. The sign and the magnitude of the aerosol direct radiative forcing at the tropopause and at the top of the atmosphere is known to be very sensitive to the vertical structure of the cloud layer. The position of the aerosol layer with respect to the cloud layer can determine the absoprtion of the aerosol in the solar spectrum (Haywood and Ramaswamy, 1998; Takemura et al., 2002). A significant characteristic of the LGM is the strong positive forcing over Northern Europe and the Arctic Ocean due to extended and continuous ice sheets and sea ice throughout the year. At the surface, the direct radiative forcing is negative almost all over the globe because the solar radiation is attenuated at the surface whether soil dust aerosols scatter or absorb it. The negative forcing is generally proportional to the column loading (Fig. 3c and d). The radiative effect is larger at LGM than for present.

Table 5 shows the annual global mean direct forcing both under the clear-sky and all-sky conditions. The negative shortwave forcing and positive longwave forcing under the all-sky condition are smaller than the clear-sky due to absorption of the multi-scattered radiation by the surrounding cloud layer as mentioned above and due to the absorption of the terrestrial radiation by clouds, respectively. A difference in the global mean direct forcing between LGM and PRE both in the shortwave and longwave radiation is approximately proportional to a difference in the emission flux and column loading (Tables 2 and 3). At LGM, the direct radiative forcing of soil dust aerosols is close to zero at the tropopause and $-0.4\,\mathrm{W\,m^{-2}}$ at the surface, compared with close to zero at the tropopause and $-0.2\,\mathrm{W\,m^{-2}}$ at the surface in present conditions.

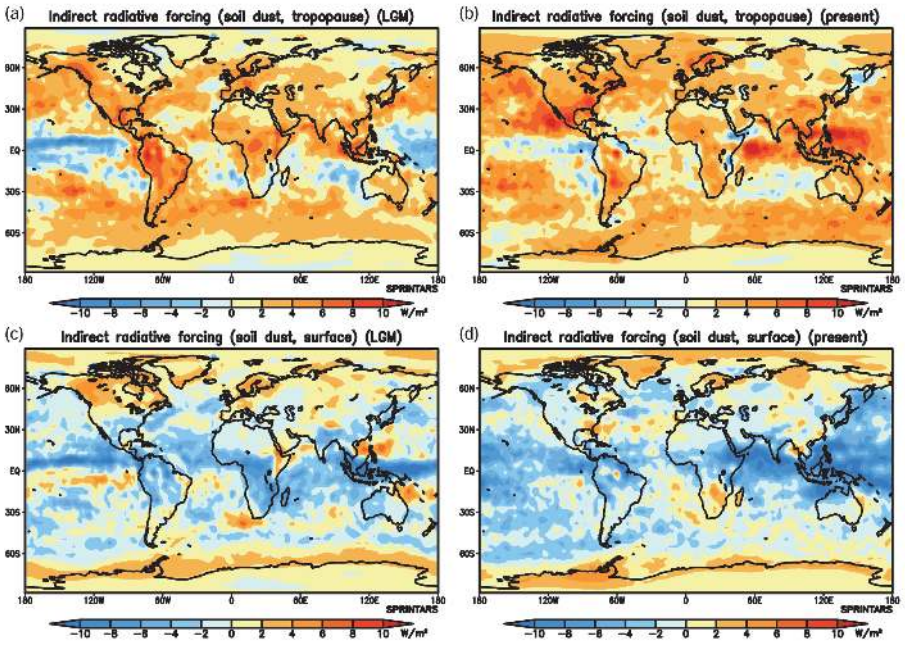


**Fig. 7.** Annual mean distributions of radiative forcing for the shortwave plus longwave radiation due to the indirect effect of soil dust aerosols at the tropopause in the **(a)** LGM and **(b)** PRE and at the surface in **(c)** LGM and **(d)** PRE.

The indirect radiative forcing of soil dust aerosols at LGM is also estimated in this study. Soil dust aerosols play an important role as ice nuclei in forming ice crystals through heterogeneous nucleation (Lohmann and Feichter, 2005), though they are not very effective in forming water cloud droplets. Details of the model parametrization of the microphysical relationship between ice crystals and aerosol particles are given in Appendix C. The indirect radiative forcing is calculated as a difference in the cloud radiative forcing between simulations with and without the dust emission. Figure 7 shows the annual mean distribution of the indirect radiative forcing due to soil dust aerosols both in LGM and PRE. Inclusion of soil dust aerosol as ice nuclei results in smaller ice crystals, which leads to a more effective absorption of the longwave radiation than scattering of the shortwave. Therefore the indirect forcing is positive at the tropopause almost over the whole globe. At the surface, on the other hand, attenuation of the shortwave radiation due to the smaller ice crystals is prominent. The indirect radiative forcing is large where the ice water content is large. The obvious difference between LGM and PRE is the large positive forcing at the tropopause and the large negative forcing at the surface in PRE, especially over the tropics because of the reduced ice crystal concentration due to inactive convection at LGM.

The global mean indirect forcing is larger in PRE at the tropopause both in the negative shortwave and positive longwave radiations than during the LGM, though the dust loading is larger at LGM (Table 6). A possible cause is the lower ice and liquid water contents in LGM conditions due to the lower temperatures than in present ones. The simulated ice water path on the global mean in LGM is 11% less than that in the present. The global mean positive value of the net indirect radiative forcing due to soil dust aerosols in LGM ($+2.0\,\mathrm{W\,m^{-2}}$) is smaller than that in PRE ($+2.9\,\mathrm{W\,m^{-2}}$), therefore atmospheric dust might contribute to the cold climate during the glacial periods through the indirect effect as well as the direct effect relative to the interglacial periods.

**Table 6.** Global and annual mean radiative forcing for the indirect effect of soil dust aerosols at the tropopause and surface in LGM and PRE. SW, LW, and SW+LW are shortwave, longwave, and shortwave plus longwave radiations, respectively.

| | Tropopause, $\mathrm{W\,m^{-2}}$ | | | Surface, $\mathrm{W\,m^{-2}}$ | | |
|---|---|---|---|---|---|---|
| | SW | LW | SW+LW | SW | LW | SW+LW |
| LGM | −2.81 | +4.83 | +2.02 | −2.42 | +1.25 | −1.17 |
| PRE | −3.91 | +6.79 | +2.88 | −3.08 | +1.03 | −2.05 |

## 5 Conclusions

In this study, global dust distribution and radiative forcings both of the direct and indirect effects at LGM are simulated by the global aerosol climate model, SPRINTARS. The

**Table A1.** Radius range, effective radius, and normalized emission strength of each size bin for soil dust aerosols in SPRINTARS.

| Radius range, μm | Effective radius, μm | Normalized emission strength |
|---|---|---|
| 0.10–0.22 | 0.13 | 0.0045 |
| 0.22–0.46 | 0.33 | 0.0290 |
| 0.46–1.00 | 0.82 | 0.1766 |
| 1.00–2.15 | 1.27 | 0.2633 |
| 2.15–4.64 | 3.20 | 0.2633 |
| 4.64–10.00 | 8.02 | 0.2633 |

global total dust flux during LGM is calculated to be about 2.4 times larger than the present flux due mainly to extended arid regions and stronger surface winds. The simulated dust deposition flux is in general agreement with estimations from ice core and marine sediment samplings. Further studies are, however, needed to solve the underestimation of the simulated dust deposition over Antarctica. Specific sensitivity studies should be designed to analyze the main factors that influence the emission, the atmospheric loading, and the deposition of soil dust aerosols. The global mean negative value of the direct radiative forcing due to soil dust aerosols at the tropopause at LGM is simulated to be larger than that in the present climate. The positive value of the indirect effect is smaller during LGM than at present. The global and annual mean radiative forcing of the direct plus indirect effects due to dust is $-0.9\,\mathrm{W\,m^{-2}}$ at the tropopause in LGM conditions relative to present ones. Therefore this study suggests that they contribute to the lower temperature during glacial compared to interglacial periods. The detailed and progressive studies with atmosphere-ocean coupled general circulation models or earth system models will be important to quantitatively analyze the effects of atmospheric dust on the climate system during glacial periods and analyze the possible feedback processes.

## Appendix A

### Emission flux of soil dust aerosols

A scheme of the emission mass flux of soil dust aerosols $F_{ed}$ in this study has been improved from the previous version of SPRINTARS (Takemura et al., 2000):

$$F_{ed} = \begin{cases} A_e C\,(|\boldsymbol{v}_{10}| - u_t)\,|\boldsymbol{v}_{10}|^2 & \text{for } |\boldsymbol{v}_{10}| \geq u_t \\ 0 & \text{for } |\boldsymbol{v}_{10}| < u_t \end{cases}, \quad \text{(A1)}$$

where $|\boldsymbol{v}_{10}|$ is the wind speed at 10-m height, $u_t$ is the threshold velocity set to be $6.5\,\mathrm{m\,s^{-1}}$, $C$ is the emission coefficient depending on the soil moisture $W_g$, snow amount $W_s$, and region defined as,

$$C = \begin{cases} C_d \frac{W_{gt} - W_g}{W_{gt}} & \text{for } W_g \leq W_{gt} \text{ and } W_s \leq W_{st} \\ 0 & \text{for others} \end{cases}, \quad \text{(A2)}$$

where $C_d$, $W_{gt}$ are the coefficient and threshold soil moisture depending on the region and $W_{st}$ is the threshold snow amount, and $A_e$ is the effective area in emitting soil dust aerosols according to Tegen et al. (2002):

$$A_e = \begin{cases} 1 - \mathrm{FPAR} & \text{for FPAR} \leq 0.25 \\ 0 & \text{for FPAR} > 0.25 \end{cases}, \quad \text{(A3)}$$

$$\mathrm{FPAR} = 1 - \exp\left(-0.5 \times \mathrm{LAI}\right), \quad \text{(A4)}$$

where FPAR is the fraction absorbed photosynthetically active radiation. SPRINTARS predicts the mass mixing ratio of soil dust aerosols dividing radii into 6 bins from 0.1 to 10 μm. Table A1 shows the normalized emission strength of each size bin based on d'Almeida and Schütz (1983). The dust emission flux is calculated at every model time step.

**Table B1.** Radius range and effective radius of each size bin for sea salt aerosols in SPRINTARS.

| Radius range, μm | Effective radius, μm |
|---|---|
| 0.100–0.316 | 0.178 |
| 0.316–1.000 | 0.562 |
| 1.000–3.160 | 1.780 |
| 3.160–10.000 | 5.620 |

## Appendix B

### Emission flux of sea salt aerosols

A scheme of the emission mass flux of sea salt aerosols $F_{es}$ in this study has been changed from the previous version of SPRINTARS (Takemura et al., 2000). The new scheme is based on Monahan et al. (1986):

$$\frac{dF_{es}}{dr} = \frac{4}{3}\pi\rho_s a\,|\boldsymbol{v}_{10}|^b\,r^{-3}\left(1 + cr^d\right) \times 10^{f\exp\left[-\{(g-\log r)/h\}^2\right]}, \quad \text{(B1)}$$

where $r$ and $\rho_s$ are the radius and density of sea salt aerosol, respectively, and $a$, $b$, $c$, $d$, $f$, $g$, and $h$ are constants according to Monahan et al. (1986). SPRINTARS predicts the mass mixing ratio of sea salt aerosols dividing radii into 4 bins from 0.1 to 10 μm (Table B1). The sea salt emission flux is calculated at every model time step.

## Appendix C

### Parameterization of interaction between aerosols and ice crystals

The latest version of SPRINTARS treats the cloud droplet number concentration $n_l$ and ice crystal number

**Table C1.** Constants for Eqs. (C3) and (C4).

| Aerosol | $a_c$, $K^{-1}$ | $b_c$ | $T_{i0}$, K |
|---|---|---|---|
| dust | 0.1014 | 0.3277 | 241.15 |
| BC | 0.00978 | 0.0913 | 232.15 |

concentration $n_i$ as prognostic variables:

$$\frac{\partial n_l}{\partial t} = R(n_l) + N_{\rm nuc} - N_{\rm sel} - N_{\rm frc} - N_{\rm fri} - \frac{n_l}{q_l}\left(Q_{\rm aut} + Q_{\rm arl} + Q_{\rm asl}\right), \quad \text{(C1)}$$

$$\frac{\partial n_i}{\partial t} = R(n_i) + N_{\rm frh} + N_{\rm frc} + N_{\rm fri} - N_{\rm agg} - \frac{n_i}{q_i} Q_{\rm asi}, \quad \text{(C2)}$$

where $R$ indicates the advection and diffusion terms, $q_l$ and $q_i$ are the in-cloud mass mixing ratios of cloud water and ice, respectively, and the time-varying terms $N$ and $Q$ with subscripts are as follows: $N_{\rm nuc}$ is the nucleation of cloud droplets, $N_{\rm frh}$ is the homogeneous freezing of supercooled aerosols, $N_{\rm frc}$ is the contact freezing, $N_{\rm fri}$ is the immersion/condensation freezing, $N_{\rm sel}$ is the self-collection of cloud droplets, $N_{\rm agg}$ is the aggregation of ice crystals, $Q_{\rm aut}$ is the autoconversion of cloud droplets, $Q_{\rm arl}$ and $Q_{\rm asl}$ are the accretion of cloud droplets by rain and snow, respectively, and $Q_{\rm asi}$ is the accretion of ice crystals by snow. The nucleation of cloud droplets $N_{\rm nuc}$ is according to Eqs. (1)–(4) in Takemura et al. (2005). The homogeneous freezing $N_{\rm frh}$ is based on Kärcher and Lohmann (2002). BC and soil dust aerosols act as IN for the heterogeneous freezing including the contact and immersion/condensation processes. Ratios of activated IN to the total number concentration of BC and dust for the contact freezing $f_{\rm frc}$ and the immersion/condensation freezing $f_{\rm fri}$ are based on Fig. 1 in Lohmann and Diehl (2006):

$$f_{\rm frc} = a_c\,(273.15 - T) - b_c\,, \quad \text{(C3)}$$

$$f_{\rm fri} = \begin{cases} \exp\left\{-\left(\frac{T_{i0}-T}{T_i}\right)^2\right\} & \text{for } T \geq T_{i0} \\ 1 & \text{for } T < T_{i0} \end{cases}, \quad \text{(C4)}$$

where $T$ is the temperature in K, $a_c$, $b_c$, $T_{i0}$ are constants depending on aerosol species (Table C1), and $T_i$=3 K. The terms of $N_{\rm frc}$ and $N_{\rm fri}$ are according to Lohmann and Diehl (2006) and Diehl et al. (2006). The deposition freezing is neglected in this study because it generally takes place at lower temperatures and higher supersaturation than the other heterogeneous freezing processes (Lohmann and Diehl, 2006). The self-collection of cloud droplets $N_{\rm sel}$ and the aggregation of ice crystals $N_{\rm agg}$ are following Lohmann et al. (1999) and Levkov et al. (1992), respectively. The Berry's parameterization (Berry, 1967) is adopted as the autoconversion of cloud droplets $Q_{\rm aut}$ (Eq. 6 in Takemura et al., 2005). The accretion of cloud droplets by rain and snow is calculated as:

$$Q_{\rm arl,asl} = F_p E_l q_l, \quad \text{(C5)}$$

where $F_p$ is the in-cloud flux of rain or snow and $E_l$ is a constant, 1.0 for rain and 0.5 by snow. The accretion of ice crystals by snow is also calculated as:

$$Q_{\rm asi} = F_p E_i q_i, \quad \text{(C6)}$$

where $E_i$ is 0.05.

*Acknowledgements.* We would like to thank the contributors of development of SPRINTARS and MIROC, DIRTMAP investigators, and anonymous reviewers. The simulation in this study was performed on the NIES supercomputer system (NEC SX-8R). This study is supported by the Grant-in-Aid for Young Scientists (18681002) of the Ministry of Education, Culture, Sports, Science, and Technology of Japan.

Edited by: Y. Balkanski

## References

Andersen, K. K., Armengaud, A., and Genthon, C.: Atmospheric dust under glacial and interglacial conditions, Geophys. Res. Lett., 25, 2281–2284, 1998.

Andreae, M. O.: Biomass burning: Its history, use, and distribution and its impact on environmental quality and global climate, in: Global Biomass Burning: Atmospheric, Climatic, and Biospheric Implications, edited by: Levine, J. S., MIT Press, Cambridge, Mass., USA, 3–21, 1991.

Basile, I., Grousset, F. E., Revel, M., Petit, J. R., Biscaye, P. E., and Barkov, N. I.: Patagonian origin of glacial dust deposited in East Antarctica (Vostok and Dome C) during glacial stages 2, 4 and 6, Earth Planet. Sc. Lett., 146, 573–589, 1997.

Berry, E. X.: Cloud droplet growth by collection, J. Atmos. Sci., 24, 688–701, 1967.

Braconnot, P., Otto-Bliesner, B., Harrison, S., Joussaume, S., Peterchmitt, J.-Y., Abe-Ouchi, A., Crucifix, M., Driesschaert, E., Fichefet, Th., Hewitt, C. D., Kageyama, M., Kitoh, A., Laîné, A., Loutre, M.-F., Marti, O., Merkel, U., Ramstein, G., Valdes, P., Weber, S. L., Yu, Y., and Zhao, Y.: Results of PMIP2 coupled simulations of the Mid-Holocene and Last Glacial Maximum – Part 1: experiments and large-scale features, Clim. Past, 3, 261–277, 2007, http://www.clim-past.net/3/261/2007/.

Chin, M., Ginoux, P., Kinne, S., Torres, O., Holben, B. N., Duncan, B. N., Martin, R. V., Logan, J. A., Higurashi, A., and Nakajima, T.: Tropospheric aerosol optical thickness from the GOCART model and comparisons with satellite and sun photometer measurements, J. Atmos. Sci., 59, 461–483, 2002.

Claquin, T., Roelandt, C., Kohfeld, K. E., Harrison, S. P., Tegen, I., Prentice, I. C., Balkanski, Y., Bergametti, G., Hansson, M., Mahowald, N., Rodhe, H., and Schulz, M.: Radiative forcing of climate by ice-age atmospheric dust, Clim. Dynam., 20, 193–202, 2003.

d'Almeida, G. A. and Schütz, L.: Number, mass and volume distributions of mineral aerosol and soils of the Sahara, J. Clim. Appl. Meteorol., 22, 233–243, 1983.

d'Almeida, G. A., Koepke, P., and Shettle, E.: Atmospheric Aerosols: Global Climatology and Radiative Forcing, A. Deepak, Hampton, Va., USA, 561 pp., 1991.

Deepak, A. and Gerber, H. G. (Eds.): Report of the experts meeting on aerosols and their climatic effects, World Meteorological Organization, Geneva, Switzerland, Rep. WCP-55, 107 pp., 1983.

Dentener, F. J., Carmichael, G. R., Zhnag, Y., Lelieveld, J., and Crutzen, P. J.: Role of mineral aerosol as a reactive surface in the global troposphere, J. Geophys. Res., 101, 22869–22889, 1996.

Diehl, K., Simmel, M., and Wurzler, S.: Numerical sensitivity studies on the impact of aerosol properties and drop freezing modes on the glaciation, microphysics, and dynamics of clouds, J. Geophys. Res., 111, D07202, doi:10.1029/2005JD005884, 2006.

Gerten, D., Schaphoff, S., Haberlandt, U., Lucht, W., and Sitch, S: Terrestrial vegetation and water balance: Hydrological evaluation of a dynamic global vegetation model, J. Hydrol., 286, 249–270, 2004.

Guenther, A., Hewitt, C. N., Erickson, D., Fall, R., Geron, C., Graedel, T., Harley, P., Klinger, L., Lerdau, M., McKay, W. A., Pierce, T., Scholes, B., Steinbrecher, R., Tallamraju, R., Taylor, J., and Zimmerman, P.: A global model of natural volatile organic compound emissions, J. Geophys. Res., 100, 8873–8892, 1995.

Harrison, S. P., Kohfeld, K. E., Roelandt, C., and Claquin, T.: The role of dust in climate changes today, at the last glacial maximum and in the future, Earth-Sci. Rev., 54, 43–80, 2001.

Harrison, S. P. and Prentice, I. C.: Climate and $CO_2$ controls on global vegetation distribution at the last glacial maximum: analysis based on palaeovegetation data, biome modelling and palaeoclimate simulations, Global Change Biol., 9, 983–1004, 2003.

Haywood, J. M. and Ramaswamy, V.: Global sensitivity studies of the direct radiative forcing due to anthrpogenic sulfate and black carbon aerosols, J. Geophys. Res., 103, 6043–6058, 1998.

Jansen, E., Overpeck, J., Briffa, K. R., Duplessy, J.-C., Joos, F., Masson-Delmotte, V., Olago, D., Otto-Bliesner, B., Peltier, W. R., Rahmstorf, S., Ramesh, R., Raynaud, D., Rind, D., Solomina, O., Villalba, R., and Zhang, D.: Palaeoclimate, in: Climate Change 2007: The Physical Science Basis, Contribution of Working Group I to the Fourth Assessment Report of the Intergovernmental Panel on Climate Change, edited by: Solomon, S., Qin, D., Manning, M., Chen, Z., Marquis, M., Averyt, K. B., Tignor, M., and Miller, H. L., Cambridge University Press, Cambridge, UK and New York, NY, USA, 2007.

Joussaume, S.: Paleoclimatic tracers: An investigation using an atmospheric general circulation model under ice age conditions 1. Desert dust, J. Geophys. Res., 98, 2767–2805, 1993.

Jouzel, J., Barkov, N. I., Barnola, J. M., Bender, M., Chappellaz, J., Genthon, C., Kotlyakov, V. M., Lipenkov, V., Lorius, C., Petit, J. R., Raynaud, D., Raisbeck, G., Ritz, C., Sowers, T., Stievenard, M., Yiou, F., and Yiou, P.: Extending the Vostok ice-core record of palaeoclimate to the penultimate glacial period, Nature, 364, 407–412, 1993.

K-1 Model Developers: K-1 coupled GCM (MIROC) description, edited by: Hasumi, H. and Emori, S., K-1 Tech. Rep. 1, 34 pp., Center for Climate System Research, University of Tokyo, Tokyo, Japan, 2004.

Kageyama, M., Laine, A., Abe-Ouchi, A., Braconnot, P., Cortijo, E., Crucifix, M., de Vernal, A., Guiot, J., Hewitt, C. D., Kitoh, A., Kucera, A., Marti, O., Ohgaito, R., Otto-Bliesner, B., Peltier, W. R., Rosell-Melé, A., Vettoretti, G., Weber, S. L., Yu, Y., and MARGO Project Members: Last Glacial Maximum temperatures over the North Atlantic, Europe and Western Siberia: A comparison between PMIP models, MARGO sea-surface temperatures and pollen-based reconstructions, Quaternary Sci. Rev., 25, 2082–2102, 2006.

Kärcher, B. and Lohmann, U.: A parameterization of cirrus cloud formation: Homogeneous freezing of supercooled aerosols, J. Geophys. Res., 107, 4010, doi:10.1029/2001JD000470, 2002.

Kaufman, Y. J., Tanré, D., Dobovik, O., Karnieli, A., and Remer, L. A.: Absorption of sunlight by dust as inferred from satellite and ground-based remote sensing, Geophys. Res. Lett., 28, 1479–1482, 2001.

Kohfeld, K. E. and Harrison, S.: DIRTMAP: The geological record of dust, Earth Sci. Rev., 54, 81–114, 2001.

Kucera, M., Rosell-Melé, A., Schneider, R., Waelbroeck, C., and Weinelt, M.: Multiproxy approach for the reconstruction of the glacial ocean surface (MARGO), Quaternary Sci. Rev., 24, 813–819, 2005.

Levkov, L., Rockel, B., Kapitza, H., and Raschke, E.: 3D mesoscale numerical studies of cirrus and stratus clouds by their time and space evolution, Beitr. Phys. Atmos., 65, 35–58, 1992.

Lohmann, U., Feichter, J., Chuang, C. C., and Penner, J. E.: Prediction of the number of cloud droplets in the ECHAM GCM, J. Geophys. Res., 104, 9169–9198, 1999.

Lohmann, U. and Feichter, J.: Global indirect aerosol effects: a review, Atmos. Chem. Phys., 5, 715–737, 2005, http://www.atmos-chem-phys.net/5/715/2005/.

Lohmann, U. and Diehl, K.: Sensitivity studies of the importance of dust ice nuclei for the indirect aerosol effect on stratiform mixed-phase clouds, J. Atmos. Sci., 63, 968–982, 2006.

Mahowald, N., Kohfeld, K., Hansson, M., Balkanski, Y., Harrison, S. P., Prentice, I. C., Schulz, M., and Rodhe, H.: Dust sources and deposition during the last glacial maximum and current climate: A comparison of model results with paleodata from ice cores and marine sediments, J. Geophys. Res., 104, 15895–15916, 1999.

Mahowald, N. M., Muhs, D. R., Levis, S., Rasch, P. J., Yoshioka, M., Zender, C. S., and Luo, C.: Change in atmospheric mineral aerosols in response to climate: Last glacial period, preindustrial, modern, and doubled carbon dioxide climates, J. Geophys. Res., 111, D10202, doi:10.1029/2005JD006653, 2006.

Masson-Delmotte, V., Kageyama, M., Braconnot, P., Charbit, S., Krinner, G., Ritz, C., Guilyardi, E., Jouzel, J., Abe-Ouchi, A., Crucix, M., Gladstone, R. M., Hewitt, C. D., Kitoh, A., LeGrande, A. N., Marti, O., Merkel, U., Motoi, T., Ohgaito, R., Otto-Bliesner, B., Peltier, W. R., Ross, I., Valdes, P. J., Vettoretti, G., Weber, S. L., Wolk, F., and Yu, Y.: Past and future polar amplication of climate change: climate model intercomparisons and ice-core constraints, Clim. Dynam., 26, 513–529, doi:10.1007/s00382-005-0081-9, 2005.

Monahan, E. C., Spiel, D. E., and Davidson, K. L.: A model of marine aerosol generation via whitecaps and wave disruption, in: Oceanic Whitecaps, edited by: Monahan, E. and Niocaill, G. M., D. Reidel, Norwell, Mass., USA, 167–174, 1986.

Nakajima, T., Tsukamoto, M., Tsushima, Y., Numaguti, A., and Kimura, T.: Modeling of the radiative process in an atmospheric general circulation model, Appl. Optics, 39, 4869–4878, 2000.

Otto-Bliesner, B. L., Schneider, R., Brady, E. C., Kucera, M., Abe-Ouchi, A., Bard, E., Braconnot, P., Crucifix, M., Hewitt, C., Kageyama, M., Marti, O., Paul, A., Rosell-Melé, A., Waelbroeck, C., Weber, S. L., Weinelt, M., and Yu, Y.: A comparison of PMIP2 model simulations and the MARGO proxy reconstruc-

tion for tropical sea surface temperatures at last glacial maximum, Clim Dynam., 32, 799–815, 2009.

Randerson, J. T., van der Werf, G. R., Collatz, G. J., Giglio, L., Still, C. J., Kasibhatla, P., Miller, J. B., White, J. W. C., DeFries, R. S., and Kasischke, E. S.: Fire emissions from C3 and C4 vegetation and their influence on interannual variability of atmospheric $CO_2$ and d13$CO_2$, Global Biogeochem. Cy., 19, GB2019, doi:10.1029/2004GB002366, 2005.

Rayner, N. A., Parker, D. E., Horton, E. B., Folland, C. K., Alexander, L. V., Rowell, D. P., Kent, E. C., and Kaplan, A.: Global analysis of sea surface temperature, sea ice, and night marine air temperature since the late nineteenth century, J. Geophys. Res., 108, 4407, doi:10.1029/2002JD002670, 2003.

Petit, J. R., Jouzel, J., Raynaud, D., Barkov, N. I., Barnola, J.-M., Basile, I., Bender, M., Chappellaz, J., Davis, M., Delaygue, G., Delmotte, M., Kotlyakov, V. M., Legrand, M., Lipenkov, V. Y., Lorius, C., Pépin, L., Rits, C., Saltzman, E., and Stievenard, M.: Climate and atmospheric history of the past 420,000 years from the Vostok ice core, Antarctica, Nature, 399, 429–436, 1999.

Sitch, S., Smith, B., Prentice, I. C., Arneth, A., Bondeau, A., Cramer, W., Kaplan, J., Levis, S., Lucht, W., Sykes, M., Thonicke, K., and Venevsky, S.: Evaluation of ecosystem dynamics, plant geography and terrestrial carbon cycling in the LPJ Dynamic Vegetation Model, Global Change Biol., 9, 161–185, 2003.

Spiro, P. A., Jacob, D. J., and Logan, J. A.: Global inventory of sulfur emissions with $1^\circ \times 1^\circ$ resolution, J. Geophys. Res., 97, 6023–6036, 1992.

Takemura, T., Okamoto, H., Maruyama, Y., Numaguti, A., Higurashi, A., and Nakajima, T.: Global three-dimensional simulation of aerosol optical thickness distribution of various origins, J. Geophys. Res., 105, 17853–17873, 2000.

Takemura, T., Nakajima, T., Dubovik, O., Holben, B. N., and Kinne, S.: Single-scattering albedo and radiative forcing of various aerosol species with a global three-dimensional model, J. Climate, 15, 333–352, 2002.

Takemura, T., Nozawa, T., Emori, S., Nakajima, T. Y., and Nakajima, T.: Simulation of climate response to aerosol direct and indirect effects with aerosol transport-radiation model, J. Geophys. Res., 110, D02202, doi:10.1029/2004JD005029, 2005.

Tanaka, T. and Chiba, M.: Global simulation of dust aerosol with a chemical transport model, MASINGAR, J. Meteorol. Soc. Japan, 83A, 255–278, 2005.

Tegen, I. and Fung, I.: Modeling of mineral dust in the atmosphere: Sources, transport, and optical thickness, J. Geophys. Res., 99, 22897–22914, 1994.

Tegen, I., Harrison, S. P., Kohfeld, K., Prentice, I. C., Coe, M., and Heimann, M.: Impact of vegetation and preferential source areas on global dust aerosol: Results from a model study, J. Geophys. Res., 107, 4576, doi:10.1029/2001JD000963, 2002.

Werner, M., Tegen, I., Harrison, S. P., Kohfeld, K. E., Prentice, I. C., Balkanski, Y., Rodhe, H., and Roelandt, C.: Seasonal and interannual variability of the mineral dust cycle under present and glacial climate conditions, J. Geophys. Res., 107, 4744, doi:10.1029/2002JD002365, 2002.

Wu, H., Guiot, J., Brewer, S., and Guo, Z.: Climatic changes in Eurasia and Africa at the last glacial maximum and mid-Holocene: reconstruction from pollen data using inverse vegetation modelling, Clim. Dynam., 29, 211–229, 2007.

Yanase, W. and Abe-Ouchi, A.: The LGM surface climate and atmospheric circulation over East Asia and the North Pacific in the PMIP2 coupled model simulations, Clim. Past, 3, 439–451, 2007,
http://www.clim-past.net/3/439/2007/.